Nano Research

ISSN 1998-0124 CN 11-5974/O4
https://doi.org/10.26599/NR.2026.94909225

Research Article

Synergistic Cu-Bi alloy sub-nanoclusters anchored on blue TiO_2 for selective CO_2 photoreduction to CH_4

Yangyang Yu[1], Yanjuan Sun[2](✉), Fan Dong[2]

[1] Research Institute for Carbon Dioxide Resource Utilization, Tianfu Yongxing Laboratory, Chengdu 610213, China

[2] School of Resources and Environment, Institute of Fundamental and Frontier Sciences, University of Electronic Science and Technology of China, Chengdu 611731, China

Nano Res., **Just Accepted Manuscript** • https://doi.org/10.26599/NR.2026.94909225

https://www.sciopen.com/journal/1998-0124 on Sep. 28, 2026

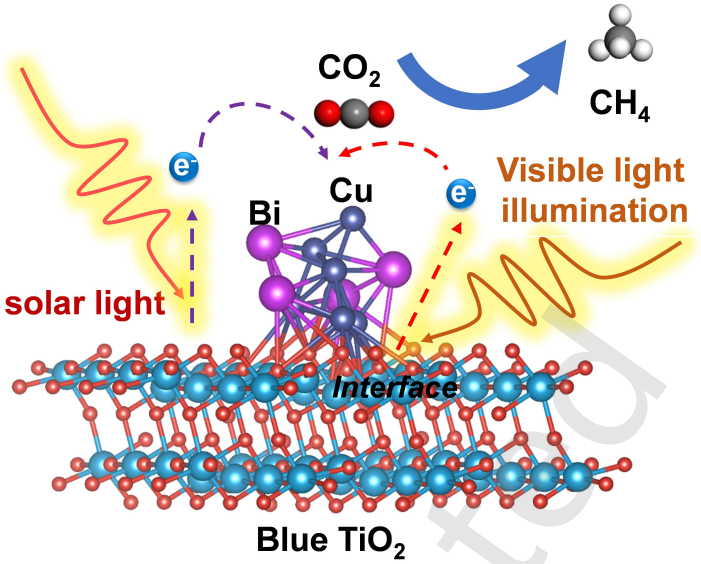
© The Authors(s)

Just Accepted

This is a "Just Accepted" manuscript, which has been examined by the peer-review process and has been accepted for publication. A "Just Accepted" manuscript is published online shortly after its acceptance,which is prior to technical editing and formatting and author proofing. Tsinghua University Press (TUP) provides "Just Accepted" as an optional and free service which allows authors to make their results available to the research community as soon as possible after acceptance. After a manuscript has been technically edited and formatted, and the page proofs have been corrected, it will be removed from the "Just Accepted" web site and published officially with volume and article number (e.g., *Nano Research*, **2025**, *18*, 94906990). Please note that technical editing may introduce minor changes to the manuscript text and/or graphics which may affect the content, and all legal disclaimers that apply to the journal pertain. In no event shall TUP be held responsible for errors or consequences arising from the use of any information contained in these "Just Accepted" manuscripts. To cite this anuscript please use its Digital Object Identifier (DOI®),which is identical for all formats of publication.

Just Accepted

TABLE OF CONTENTS



Based on Cu-Bi alloy sub-nanocluster and defect interface engineering, this study builds unique interfacial states (IFS) via strong alloy-support dielectric coupling to generate visible-light hot electrons and boost photogenerated charge separation. The atomic electronic synergism within Cu-Bi sub-nanoclusters stabilizes metallic active sites and reduces the energy barrier of CO_2 adsorption, enabling high-efficiency and ultra-selective photocatalytic conversion of CO_2 to CH_4 over monometallic cocatalyst modified blue TiO_2.

Just Accepted

Research Article

Synergistic Cu-Bi alloy sub-nanoclusters anchored on blue TiO_2 for selective CO_2 photoreduction to CH_4

Yangyang Yu [1], Yanjuan Sun [2] ✉, Fan Dong [2]

[1] *Research Institute for Carbon Dioxide Resource Utilization, Tianfu Yongxing Laboratory, Chengdu 610213, China*

[2] *School of Resources and Environment, Institute of Fundamental and Frontier Sciences, University of Electronic Science and Technology of China, Chengdu 611731, China*

Received: 12 July 2026; **Revised:** 27 September 2026; **Accepted:** 28 September 2026

✉ Address correspondence to sunyj@uestc.edu.cn

Cite this article: *Nano Research*, 2026, 19, 94909225 https://doi.org/10.26599/NR.2026.94909225

ABSTRACT: Photocatalytic CO_2 reduction to CH_4 using H_2O offers a sustainable route for solar fuel production but remains challenged by the lack of non-noble-metal cocatalysts that are both efficient and selective. Herein, we report a stepwise photodeposition strategy to anchor Cu-Bi alloy sub-nanoclusters (ASNCs, 0.84 ± 0.12 nm) on blue TiO_2 (BT) for CO_2 photoreduction. The optimal $Bi_{0.4}Cu_{0.6}$/BT catalyst achieves a CH_4 evolution rate of 94.4 μmol g^{-1} h^{-1} with 96.9% selectivity under simulated solar irradiation, substantially outperforming monometallic Cu/BT and Bi/BT. The synergistic interaction between Cu and Bi can inhibit the aerial oxidation of metallic Cu^0 and Bi^0, accelerate the separation of photogenerated electron-hole pairs, and facilitate the adsorption and activation of CO_2. Meanwhile, strong interfacial dielectric coupling between the ASNCs and BT support creates interface states (IFS), which enables visible-light-driven hot electron injection, thereby significantly enhancing the charge separation efficiency and overall photocatalytic activity. Furthermore, the Cu-Bi alloy substantially lowers the Gibbs free energy barrier for CO_2 adsorption over Cu active sites and establishes a thermodynamically favorable pathway for stepwise hydrogenation of CO_2 toward CH_4. This work establishes a non-noble-metal alloy sub-nanocluster strategy on defect-engineered TiO_2 for efficient and selective CO_2-to-CH_4 photoreduction.

KEYWORDS: Cu-Bi alloy sub-nanoclusters, blue TiO_2, interface states, synergistic interaction, CH_4 selectivity

Just Accepted

1.Introduction

Photocatalytic conversion of carbon dioxide (CO_2) and water (H_2O) to value-added green fuels is believed to be an effective strategy for promoting sustainable development in society because it can utilize sunlight and H_2O to reduce greenhouse gases and alleviate energy shortages[1-4]. Excellent CO_2 reduction photocatalysts require strong CO_2 adsorption ability, high solar light utilization efficiency, high charge separation efficiency, high redox potential, and proper binding ability with reaction intermediates[5]. However, it is difficult for a single semiconductor catalyst to meet all of the above requirements. Therefore, metal cocatalysts are usually loaded on the surface of semiconductors for photocatalytic CO_2 reduction[6, 7].

Cu has been considered as one of the most attractive cocatalysts for CO_2 photoreduction as a result of its optimal binding energy with reaction intermediates[8]. However, the semiconductor catalyst loaded by single-component Cu species still cannot obtain excellent photocatalytic CO_2 reduction performance [9-11]. Recently, some work has focused on the binary combinations of Cu-noble metal cocatalysts in photocatalytic CO_2 reduction [12-16]. These successful cases show that the photocatalytic CO_2 reduction activities of Cu-noble metal composite cocatalysts are much higher than those of single metal cocatalysts. However, the low abundance and high price of these precious metals make it difficult to achieve large-scale applications [17]. Recently, Bi as a cocatalyst for photocatalytic CO_2 reduction has attracted increasing attention [18, 19]. In addition, some researchers have found that co-loading Bi and Cu on a semiconductor can significantly improve the photocatalytic CO_2 reduction activity of the catalysts [20]. However, this separate co-loading makes it difficult to create synergistic effects between Cu and Bi, and therefore the enhancement of catalyst activity is limited. We speculate that loading Cu and Bi on the catalyst in the form of an alloy can effectively enhance the photocatalytic activity of the catalyst, because the interaction of the two different metals in the alloy may be able to promote the separation of photogenerated electrons, enhance the adsorption of CO_2, and lower the energy barrier of the CO_2 reduction reaction.

It has been well demonstrated that the catalytic activity of metal nanoparticles can be significantly improved by reducing their size [21, 22]. For example, the d-band center of Cu clusters gradually shifts upward as their size decreases, which enhances the adsorption strength of CO* and H* intermediates, thus inhibiting hydrogen evolution reaction and boosting the production of CH_4 [23, 24]. When the size of metal particles is reduced to sub-nanoclusters (SNCs, < 1 nm), their electronic properties are different from those of nanoparticles (2–100 nm) and nanoclusters (1–2 nm), and more metal/carrier interfaces can also be constructed, resulting in catalysts with more excellent catalytic performance [25, 26]. Furthermore, studies have revealed that strong interfacial dielectric coupling between metal or alloy sub-nanoclusters (ASNCs) and TiO_2 can lead to the formation of an interface state (IFS), which enables the direct generation of hot electrons in TiO_2 under visible-light irradiation. These hot electrons subsequently migrate to the metal or alloy surface, significantly enhancing the CO_2 photoreduction activity of the catalyst [27–30]. Therefore, loading Cu-Bi ASNCs on TiO_2 catalysts for photocatalytic CO_2 reduction is a feasible and innovative strategy. However, to

Just Accepted

the best of our knowledge, no relevant studies have been reported so far.

Herein we report a stepwise photodeposition strategy for the synthesis of Cu-Bi ASNCs on Blue TiO_2 (BT), denoted as Bi_xCu_{1-x}/BT (x=0, 0.2, 0.4, 0.6 and 1.0 corresponding to at% Bi), for photocatalytic CO_2 reduction with H_2O. The optimized $Bi_{0.4}Cu_{0.6}$/BT catalyst delivers a CH_4 production rate of 94.4 μmol g^{-1} h^{-1} with 96.9% selectivity under simulated solar irradiation. Mechanistic investigations reveal that the synergistic interaction between Cu and Bi can inhibit the aerial oxidation of metallic Cu^0 and Bi^0, accelerate the separation of photogenerated electron-hole pairs, and facilitate the adsorption and activation of CO_2. More importantly, the strong interfacial dielectric coupling between the Cu-Bi ASNCs and the BT support generates an interface state (IFS) within the bandgap of BT, which enables the direct generation of hot electrons under visible-light excitation. Moreover, the Cu-Bi alloy substantially lowers the Gibbs free energy barrier for CO_2 adsorption over Cu active sites and establishes a thermodynamically favorable pathway for stepwise hydrogenation of CO_2 toward CH_4. This work establishes a non-noble-metal alloy sub-nanocluster strategy on defect-engineered TiO_2 for efficient and selective CO_2-to-CH_4 photoreduction.

2. Experimental

2.1. Synthesis of Blue TiO_2 (BT)

1.00 g of TiO_2 (P25, 1.0 g) was mixed with 0.15g of sodium borohydride ($NaBH_4$, AR, Sinopharm Chemical Reagent Co., Ltd.) by grinding. Subsequently, the mixture was then placed in a quartz tube furnace and heated at 350 °C for 0.5 h under an argon atmosphere. The obtained samples were washed 6 times with ethanol and deionized water, respectively, and then dried under vacuum at 80 °C.

2.2. Synthesis of Bi_xCu_{1-x}/BT

Bi_xCu_{1-x}/BT was synthesized via a stepwise photodeposition method. Typically, 1.00 g of BT was dispersed in 150 mL of ethylene glycol (AR, Aladdin Chemical Reagent Co., Ltd.) and ultrasonicated for 10 min to promote the dispersion of TiO_2. The suspension was then purged with argon for 30 min to eliminate dissolved O_2. Variable amounts of $Bi(NO_3)_3 \cdot 5H_2O$ solution (5.00 g/L, 99.99% metals basis, Aladdin Chemical Reagent Co., Ltd.) were added to the above suspension under vigorous stirring. Subsequently, the suspension was immediately illuminated under a mercury lamp (300 W) for 1 h. Next, a solution of copper nitrate trihydrate (5.00 g/L, 99.99% metal content, Aladdin Chemical Reagent Co., Ltd.) with varying amounts was added to the suspension, followed by another hour of irradiation. Finally, the samples were washed with deionized water and dried in a vacuum oven at 80 °C. The resulting samples were identified as Bi_xCu_{1-x}/BT, where x = 0, 0.2, 0.4, 0.6 and 1.0 corresponding to theoretically calculated at% Bi.

2.3. Characterization

The high-angle annular darkfield scanning transmission electron microscopy (HAADF-STEM, FEI Titan Themis 60-30) was used to observe morphology and structure of the catalysts. The crystal phases of the catalysts were characterized by X-ray diffraction (XRD) patterns with CuK-α radiation (Model D/max RA, Rigaku Co.). The X-ray photoelectron spectroscopy (XPS, Thermo ESCALAB 250) was used to investigate the surface properties of the catalysts. The photoelectric properties of catalysts were measured by UV-vis DRS (UV-2450, Shimadzu, Japan). Electron spin resonance (ESR) experiments were conducted on a JES FA200 spectrometer, with 2,2,6,6-tetramethylpiperidine-1-oxyl (TEMPO) used to trap electron spins and

Just Accepted

5,5-dimethyl-1-pyrroline-N-oxide (DMPO) used to trap radical spins.

2.4. *In situ* FT-IR measurement

In situ FT-IR test was performed using the ConcentratIR 2TM (Harrick) in a Bruker Vertex 70v spectrometer equipped with an MCT detector. Firstly, the photocatalyst coated on the diamond ATR crystal surface was treated in a vacuum for 30 min to remove the adsorbed water molecules. Then, H_2O vapor and CO_2 were introduced into the gas pipeline until the atmospheric pressure. After 30 min in the dark, the photocatalyst was irradiated for 30 min and IR spectra were recorded simultaneously and repeatedly with a certain time interval.

2.5. CO_2 photoreduction tests

The CO_2 reduction performance of the photocatalyst was tested in a Labsolar-6A closed-cycle system (Beijing Perfectlight Technology Co., Ltd.). 10.0 mg of the photocatalyst was uniformly dispersed in deionized water via ultrasonication and then loaded onto the surface of a microporous membrane with a radius of 2.0 cm (geometric area: 12.57 cm², fully exposed to the incident beam without shading). The microporous membrane loaded with the catalyst was placed on a tray inside the reactor. After sealing, the reactor underwent three cycles of "vacuum pumping-filling with CO_2" to completely displace the residual O_2 or other impurities. Subsequently, 0.15 mL of water was injected into the reactor under vacuum to allow the water to fully vaporize. CO_2 was then introduced to adjust the system pressure to 90 kPa (slightly below atmospheric pressure) to maintain reactor airtightness. Finally, the light source (a 300 W Xe lamp equipped with an AM1.5 filter) was turned on to conduct the reaction at a light intensity of 500 mW cm^{-2} (measured using a CEL-NP2000 full-spectrum optical power meter (Beijing CEAULIGHT Technology Co., Ltd.) equipped with a φ10 mm photoelectric detection probe (sensitive area: 0.75 cm^2); calibration wavelength range: 190-11000 nm with direct-read capability in 190-2500 nm (uniformity 2.7%); power range: 0-2000 mW cm^{-2}; resolution: 1 μW; uncertainty: <±5%; the probe was placed at the reactor window position perpendicular to the film surface, and light uniformity was confirmed within ±5% over a 2×2 cm^2 grid by multi-point scanning). During illumination, gaseous products were analyzed hourly using gas chromatography. The selectivity of CH_4 (%) is calculated according to the number of electrons required for each product in the photocatalytic CO_2 reduction process, using the following formula: CH_4 selectivity (%) = $[8\varphi(CH_4)]/[8\varphi(CH_4) + 12\varphi(C_2H_4) + 2\varphi(H_2) + 2\varphi(CO)] \times 100\%$. DFT details are provided in the Supporting Information. Each photocatalytic test was independently repeated three times with freshly prepared catalyst films under identical conditions, and the product formation rates are reported as the average values of the three parallel measurements. The error bars represent the standard deviation of the three independent measurements.

3. Results and discussion

3.1. The morphology, structure, and composition of catalysts

The structure, composition, and distribution of Cu, Bi monometallic species and Cu-Bi alloy on the BT support were analyzed using HAADF, HAADF-STEM, and TEM elemental mapping techniques. The HAADF results indicate that small Bi and Cu SNCs are uniformly dispersed on the surfaces of Bi/BT and Cu/BT catalysts, respectively (Figure S1). This is due to the relatively low reduction potentials of Bi (Bi^{3+}/Bi, E^0 = +0.32 V) and Cu

Just Accepted

(Cu^{2+}/Cu, E^0 = +0.34 V), which prevent their rapid growth under the action of photogenerated electrons from BT [31, 32]. The HAADF-STEM images show that the metal SNCs in $Bi_{0.4}Cu_{0.6}$/BT are uniformly anchored on the surface of BT, with a very small size and a narrow size distribution of 0.84 ± 0.12 nm (Figures 1a, b). In addition, the STEM elemental mapping (circled region in Figure 1c) further confirms the formation of Cu-Bi ASNCs in $Bi_{0.4}Cu_{0.6}$/BT, with a higher Cu content than Bi in these ASNCs (Figure 1c).

Further evidence for alloying is provided by the Z-contrast analysis of the aberration-corrected HAADF-STEM images (Figure 1a and Figure S2). In HAADF imaging, the intensity scales approximately as Z1.7, enabling direct discrimination of elements with vastly different atomic numbers [33]. Given the large atomic number difference between Bi (Z = 83) and Cu (Z = 29), phase-separated pure Bi and pure Cu SNCs would manifest as drastically contrasting brightness: Bi clusters would appear as intensely bright white spots, whereas Cu clusters would be markedly dimmer. However, the SNCs in Bi0.4Cu0.6/BT display relatively uniform contrast without the distinct bimodal brightness distribution expected for phase-separated species (Figure 1a and Figure S2). This uniform Z-contrast is consistent with atomic-scale mixing within Cu-Bi ASNCs rather than adjacent monometallic particles. Such Z-contrast behavior has been previously employed to distinguish alloyed structures from phase-separated mixtures in bimetallic sub-nanocluster systems[29].

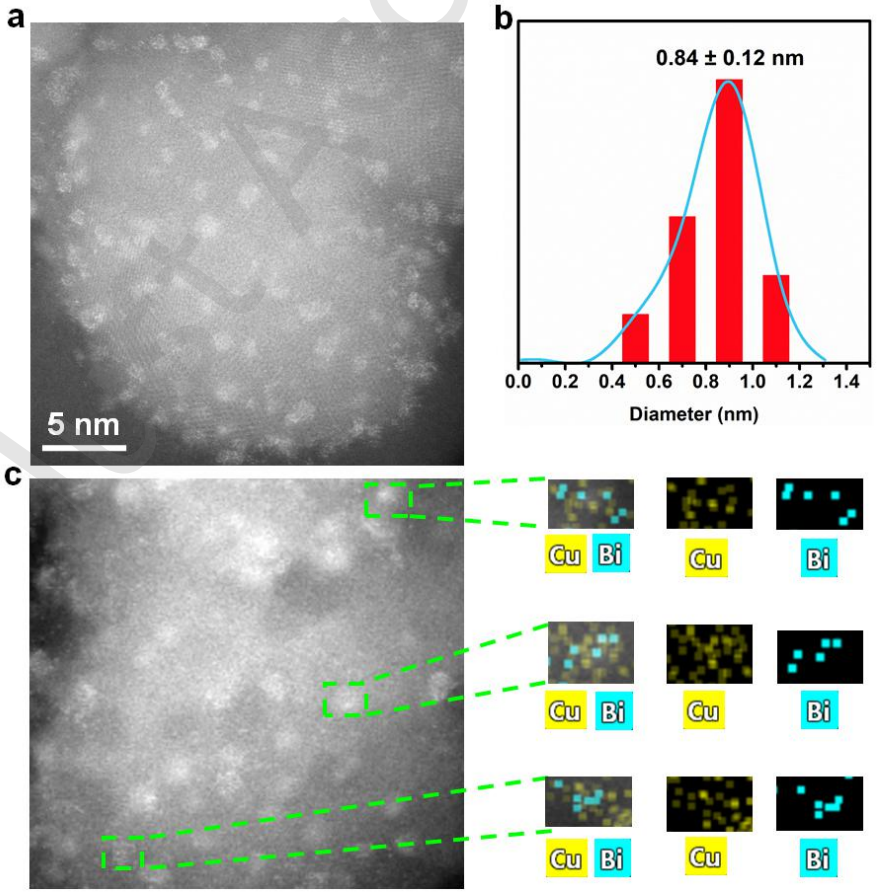


Figure 1. HAADF-STEM images (a) of $Bi_{0.4}Cu_{0.6}$/BT. Size distributions (b), and STEM elemental mapping

images (c) of Cu-Bi ASNCs.

The crystalline phase structure of the catalyst was further characterized by XRD. As shown in Figure S3a, the diffraction peaks of pristine TiO_2 can be attributed to the coexistence of anatase and rutile phases of TiO_2 (JCPDS 38-0741 and JCPDS 21-1276). The diffraction peak positions of BT coincide with those of TiO_2, but the peak intensities are significantly lower than those of TiO_2. This may be attributed to a high concentration of oxygen vacancies in BT, which induce lattice distortion and reduce crystalline integrity, thereby diminishing the diffraction peak intensity. No characteristic diffraction peaks of metallic Cu or Bi are observed in the XRD patterns of Cu/BT, Bi/BT and Bi_xCu_{1-x}/BT, confirming the high dispersion of Cu, Bi, and Cu-Bi alloy on the BT support, consistent with HAADF and HAADF-STEM results (Figure S1 and Figure 1). Figure S3b shows the UV-vis DRS of the catalyst. TiO_2 does not show an absorption peak in the visible light region, while the BT sample exhibits significant light absorption in the visible light region. This is mainly due to the presence of a large number of disordered surface layers, Ti^{3+} and oxygen vacancies in BT, which leads to a reduction in the band gap [34]. The visible light absorption of the catalysts slightly decreased after loading Cu, Bi, and Cu-Bi alloy. This may be attributed to the fact that sub-nanometer sized Cu, Bi, and Cu-Bi alloy species possess no intrinsic absorption capability in the visible light range, while their presence on the BT surface slightly modifies BT's original visible light absorption properties. Notably, Cu nanoparticles are well documented to exhibit localized surface plasmon resonance (LSPR) in the visible light region, which typically enhances visible-light absorption[35]. However, in the present work, the visible-light absorption decreases rather than increases after loading Cu, Bi, or Cu-Bi alloy, suggesting that the conventional LSPR effect of Cu is absent here. This can be rationalized by the size-dependent nature of LSPR: pronounced LSPR generally requires Cu nanoparticles larger than ~5 nm, whereas the Cu species in this work exist as Cu-Bi ASNCs with an average size of only 0.84 ± 0.12 nm (Figures 1a, b and S1), far below the critical threshold for collective electron oscillations. At this sub-nanometer scale, severe surface scattering effectively damps the plasmonic oscillations, rendering the Cu LSPR negligible.

XPS was used to study the chemical states and interactions of Cu and Bi loaded on the surface of the catalyst. The $Bi4f_{5/2}$ spectrum of the Bi/BT sample exhibits two characteristic peaks corresponding to Bi $4f_{5/2}$ and Bi $4f_{7/2}$, with binding energies located at 164.2 eV and 159.0 eV, respectively, which are attributed to the trivalent bismuth (Bi^{3+}) state (Figure 2a) [36]. This observation results from the complete oxidation of Bi SNCs deposited on the BT surface into Bi_2O_3 during prolonged air exposure prior to XPS characterization [37]. In contrast, for $Bi_{0.4}Cu_{0.6}$/BT, the Bi $4f_{5/2}$ and Bi $4f_{7/2}$ peaks show a negative shift of 0.5 eV to 163.7 eV and 158.4 eV, respectively (Figure 2a). This demonstrates that the Cu in Cu-Bi ASNCs enhances the air stability of Bi sub-nanoclusters, effectively preventing their oxidation during extended air exposure. The Cu 2p binding energy peaks at 952.0 eV and 932.3 eV for the Cu/BT are assigned to Cu $2p_{1/2}$ and Cu $2p_{3/2}$ of Cu^+ and/or Cu^0 species, respectively (Figure 2b) [38]. However, for the $Bi_{0.4}Cu_{0.6}$/BT, the characteristic peaks of Cu $2p_{1/2}$ and Cu $2p_{3/2}$ exhibit negative shifts to

Just Accepted

951.1 eV and 931.4 eV, respectively (Figure 2b). This observation indicates that the Cu-Bi interaction within the ASNCs significantly enhances the stability of Cu^0 species.

The enhanced air stability of Cu^0 and Bi^0 in the ASNCs can be understood from the electronic structure perspective. The work function of Cu (~4.6 eV) is higher than that of Bi (~4.2 eV), driving electron transfer from Bi to Cu upon alloying and increasing the electron density of the Cu sites[39]. Meanwhile, the electronegativity of Cu (1.90 Pauling) is slightly lower than that of Bi (2.02 Pauling), and alloying induces a downshift of the d-band center relative to the Fermi level[40]. This electronic modification weakens the adsorption of O_2 on both Cu and Bi sites, thereby suppressing surface oxidation under ambient conditions[41]. Such anti-oxidation behavior is consistent with reports on bimetallic sub-nanoclusters, where electronic coupling between dissimilar metals stabilizes the zero-valent state against aerial oxidation[13, 29].

Since XPS spectra cannot effectively distinguish between Cu^+ and Cu^0, Cu LMM X-ray Auger electron spectroscopy (Cu LMM Auger) was employed to differentiate these chemical states. As shown in Figure 2c, the two overlapping peaks at 564.4 eV and 566.9 eV are assigned to the kinetic energies of Cu^0 and Cu^+, respectively [42]. For $Bi_{0.4}Cu_{0.6}$/BT, the peak area of Cu^0 is significantly larger than that of Cu^+, demonstrating that the majority of Cu exists in the metallic state (Cu^0) within the Cu-Bi nanoclusters.

The substantial mutual binding energy shifts observed in the XPS spectra provide additional compelling evidence for alloy formation. For $Bi_{0.4}Cu_{0.6}$/BT, the Bi $4f_{7/2}$ peak shifts negatively by ~0.5 eV relative to Bi/BT, while the Cu $2p_{3/2}$ peak shifts negatively by ~0.9 eV relative to Cu/BT. Such large reciprocal shifts cannot be rationalized by simple spatial proximity or a physical mixture of separate Cu and Bi domains, instead, they reflect substantial intermetallic electronic coupling and charge redistribution within the alloy cluster[29, 39]. According to the work function difference (Cu ~4.6 eV vs. Bi ~4.2 eV) and electronegativity considerations, alloying induces electron transfer from Bi to Cu, increasing the electron density of Cu sites and concurrently modifying the electronic environment of Bi atoms through lattice-level hybridization. This magnitude of binding energy reorganization is characteristic of true alloy formation rather than adjacent monometallic particles [41].

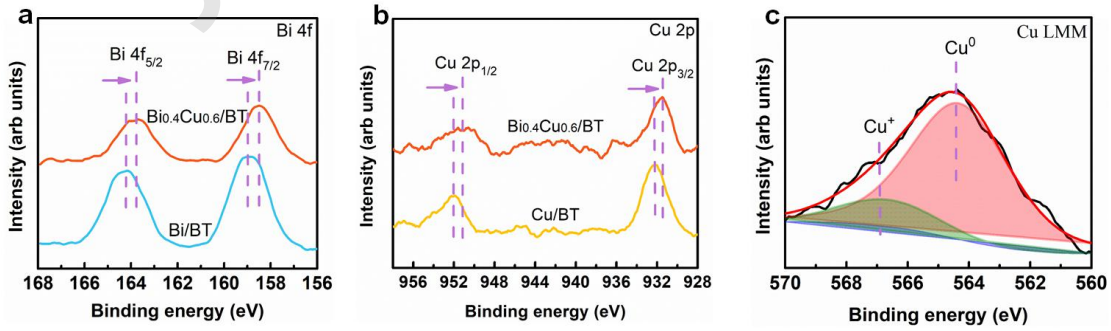


Figure 2. XPS spectra for Bi4f (a) and Cu 2p (b) of the catalysts. Cu LMM Auger spectra (c) of

Just Accepted

$Bi_{0.4}Cu_{0.6}$/BT.

3.2. The photocatalytic CO_2 reduction performance of the catalysts

The photocatalytic CO_2 reduction performance of the catalysts was evaluated under AM 1.5G simulated solar irradiation, and the results are shown in Figure 3. Figure 3a displays the average formation rates of CH_4, CO, and H_2 over different catalysts under simulated solar irradiation (AM 1.5G, 500 mW cm^{-2}). As shown in Figure 3a, TiO_2 exhibits low CO_2 photoreduction activity, primarily due to its wide bandgap that results in limited solar spectrum absorption and insufficient active sites for effective CO_2 adsorption and activation. In contrast, BT demonstrates significantly enhanced photocatalytic CO_2 reduction performance. This improvement is achieved through the introduction of oxygen vacancies and the formation of a disordered surface structure, which collectively narrow the bandgap to extend visible-light response range. Simultaneously, the engineered defect sites not only promote CO_2 molecule adsorption and activation but also markedly enhance the separation and transport efficiency of photogenerated charge carriers, ultimately leading to superior catalytic performance. When loaded with Cu or Bi SNCs, the CO_2 photoreduction activity of BT catalysts is significantly enhanced, which can be attributed to the promoted separation of photogenerated electrons and holes by Cu or Bi SNCs, as well as their role as active sites facilitating CO_2 activation. Notably, the CH_4 formation rate of Cu/BT catalysts is substantially higher than that of Bi/BT catalysts, while its CO formation rate is considerably lower. This indicates that Cu SNCs are more conducive to promoting CH_4 generation compared to Bi SNCs. Bi_xCu_{1-x}/BT (x = 0.2, 0.4, 0.6) exhibits significantly enhanced CO_2 photoreduction activity compared to Bi/BT and Cu/BT. This enhancement may be attributed to the Cu-Bi interaction within the Cu-Bi ASNCs, which stabilizes both Cu and Bi, effectively promoting the separation of photogenerated electrons and holes and facilitating CO_2 adsorption and activation.

Among the Bi_xCu_{1-x}/BT (x = 0.2, 0.4, 0.6) catalysts, $Bi_{0.4}Cu_{0.6}$/BT achieves the highest photocatalytic activity with formation rates of 94.4, 4.3 and 7.7 μmol g^{-1} h^{-1} for CH_4, CO and H_2, respectively. This CH_4 formation rate substantially exceeds that of the Cu/BT (36.2 μmol g^{-1} h^{-1}) and Bi/BT (18.8 μmol g^{-1} h^{-1}) catalysts. To verify that the enhanced photocatalytic activity arises from a true Cu-Bi alloying effect rather than the simple combination of individual Cu and Bi species, a physically mixed control sample (denoted as Cu/BT + Bi/BT) was prepared and evaluated under identical conditions. The total catalyst loading was fixed at 10 mg, consisting of 6 mg Cu/BT and 4 mg Bi/BT, consistent with the Bi/Cu stoichiometry in $Bi_{0.4}Cu_{0.6}$/BT, and both Cu/BT and Bi/BT contain identical metal loadings. As shown in Figure S4, the physical mixture exhibits a CH_4 formation rate of 32.4 μmol g^{-1} h^{-1}, whereas $Bi_{0.4}Cu_{0.6}$/BT achieves 94.4 μmol g^{-1} h^{-1}. The CH_4 formation rate of the alloy catalyst is 2.9 times that of the physical mixture, confirming that the superior CO_2 photoreduction performance is attributable to the synergistic alloying effect within the Cu-Bi ASNCs, rather than to the additive contributions of separately deposited Cu and Bi species. The selectivity of CH_4 reaches as high as 96.9% (Figure 3b), indicating that the surface photogenerated electrons are preferentially involved in the CH_4 formation

Just Accepted

reaction. Moreover, although the generation of O_2 can be detected (which should be attributed to the oxidation of H_2O by photogenerated holes), the formation rate of O_2 cannot be accurately determined due to the inability of the reaction system to achieve absolute airtightness. This allows O_2 from the air to infiltrate the reaction system, significantly interfering with the O_2 detection results.

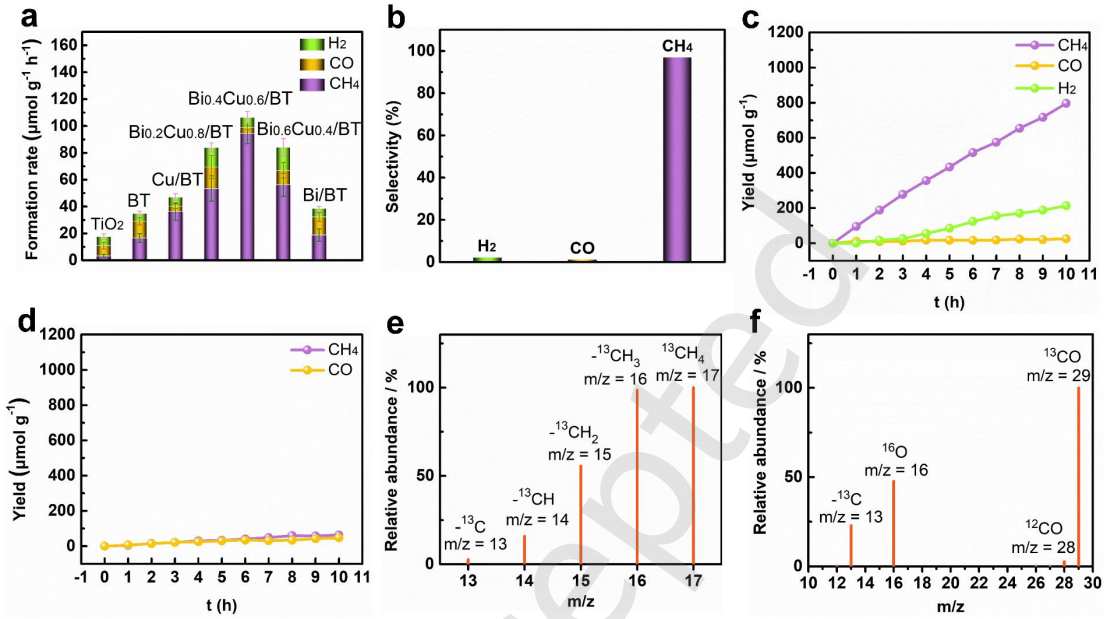


Figure 3. CH_4, H_2 and CO formation rates of the catalysts under 5 h simulated solar (AM 1.5G) irradiation (a). Data are presented as the average of three independent measurements, and the error bars represent the standard deviation. The selectivity of CH_4, CO and H_2 over $Bi_{0.4}Cu_{0.6}$/BT (b). Long-time photocatalytic stability of $Bi_{0.4}Cu_{0.6}$/BT for 10 h (c). Time-dependent CH_4 and CO evolution over $Bi_{0.4}Cu_{0.6}$/BT in wet Ar (d). GC-MS spectra of CH_4 (e), and CO (f) from the photocatalytic reduction of $^{13}CO_2$ over $Bi_{0.4}Cu_{0.6}$/BT.

To further investigate the stability of the $Bi_{0.4}Cu_{0.6}$/BT catalyst in the photocatalytic CO_2 reduction reaction, a 10 h stability test was conducted. As shown in Figure 3c, the target product CH_4 increases linearly with irradiation time, demonstrating that $Bi_{0.4}Cu_{0.6}$/BT exhibits excellent stability during a single continuous run. Moreover, repeated cycling tests show that the catalyst maintains stable CH_4 production over three consecutive 10 h cycles (30 h in total, Figure S5), with negligible activity decay between cycles. Post-reaction HAADF images (Figure S6) reveal that the Cu-Bi ASNCs retain a comparable sub-nanometer size and uniform dispersion on the BT surface, with no discernible increase in cluster size, aggregation, or sintering after prolonged operation. ESR analysis (Figure S7) further indicates that the oxygen vacancy concentration is well preserved after three cycles. These results collectively substantiate the robust structural and chemical durability of $Bi_{0.4}Cu_{0.6}$/BT. The detection of only trace amounts of CH_4 and CO in the control experiments under a wet argon atmosphere proves that CO_2 is the primary carbon source for the generation of these products (Figure 3d). Isotopic labeling experiments with $^{13}CO_2$ were performed to trace the carbon source. The mass spectra (Figures 3e and 3f) revealed that the carbon in CH_4 and CO products is predominantly derived from CO_2, as evidenced by their agreement

Just Accepted

with the spectra of the ^{13}C-labeled standards ($^{13}CH_4$ and ^{13}CO).

3.3. Photoelectrochemical properties of the catalysts

The critical dependence of CO_2 photoreduction activity on the catalyst originates from the generation and migration efficiency of photogenerated electrons. Accordingly, the surface concentration of these electrons was probed under simulated solar irradiation using TEMPO as an electron capture agent [43], as shown in Figure 4a. The BT catalyst exhibits a greater TEMPO consumption rate than TiO_2, which can be attributed to its abundant oxygen vacancies. These vacancies enhance the absorption of simulated solar light, leading to a higher yield of photogenerated electrons. The deposition of Cu or Bi SNCs onto the surface of the BT catalyst resulted in a significant acceleration of the TEMPO consumption rate. This enhancement is attributed to the fact that Cu and Bi species act as electron acceptors, which effectively capture electrons, thereby promoting the separation and migration of photogenerated electron-hole pairs. The consumption rate of TEMPO on $Bi_{0.4}Cu_{0.6}$/BT is significantly faster than that on Cu/BT and Bi/BT, indicating that $Bi_{0.4}Cu_{0.6}$/BT possesses a superior ability to generate and separate photogenerated electrons. This enhancement originates from two primary mechanisms: First, the interaction between Cu and Bi in the Cu-Bi ASNCs enhances the stability of the alloy, allowing it to remain in the metallic state more easily under ambient conditions. Since the work function of the metallic Cu-Bi alloy (4.2-4.5 eV) is higher than that of BT (4.2 eV) [44, 45], the generated photogenerated electrons rapidly migrate to the surface of the Cu-Bi ASNCs, thereby significantly increasing the surface electron density of the catalyst. Second, the strong interfacial dielectric coupling between the Cu-Bi ASNCs and the BT support facilitates the formation of an interfacial field (IFS), enabling BT to directly generate hot electrons under visible-light irradiation, which consequently enhances the overall yield of photogenerated electrons [27-29]. In addition, under simulated solar irradiation, $Bi_{0.4}Cu_{0.6}$/BT produces more superoxide ($\bullet O^{2-}$) and hydroxyl ($\bullet OH$) radicals than other catalysts (Figure S8). This result further confirms that $Bi_{0.4}Cu_{0.6}$/BT can generate and separate the largest number of photogenerated electrons and holes, and that these charge carriers possess sufficiently high reduction and oxidation potentials to participate in the subsequent redox reactions [16].

To directly evaluate the separation and migration efficiency of photogenerated charge carriers, transient photocurrent density measurements were performed under intermittent simulated solar irradiation at a bias voltage of 0 V vs. Ag/AgCl (Figure 4b). Under each illumination, all of the samples exhibit prompt and reproducible photocurrent responses, indicating stable photoelectronic properties of the catalysts. The photocurrent density of $Bi_{0.4}Cu_{0.6}$/BT is significantly higher than those of Cu/BT and Bi/BT, implying that the Cu-Bi ASNCs effectively promote the separation of photogenerated electron-hole pairs and accelerate the directional transfer of electrons to the cluster surface. Moreover, the photocurrent trends of the samples are consistent with their TEMPO consumption rates and photocatalytic activities, confirming that the synergistic Cu-Bi interaction maximizes the surface electron density available for CO_2 reduction.

The photoelectrochemical properties were further investigated by electrochemical

Just Accepted

impedance spectroscopy (EIS), and the Nyquist plots were used to analyze the impedance spectra (Figure 4c). In the Nyquist plots, the imaginary component usually represents the capacitive parameter, the real component represents the ohmic parameter, and the radius of the semicircle is related to the charge transfer resistance [46]. The impedance data were fitted to the equivalent circuit (inset of Figure 4c), which included the solution resistance (R_1), charge-transfer resistance (R_2), and constant phase element (CPE_1). The charge-transfer resistance values (R_2) were determined to be 20002 Ω for Bi/BT, 8989 Ω for Cu/BT, and 1151 Ω for $Bi_{0.4}Cu_{0.6}$/BT, respectively. The substantially reduced charge-transfer resistance of $Bi_{0.4}Cu_{0.6}$/BT relative to its monometallic counterparts indicates that the Cu-Bi ASNCs significantly reduce the interfacial charge-transfer barrier and facilitate the rapid migration of photogenerated electrons from BT to the alloy active sites. This result provides solid evidence for the enhanced charge separation efficiency in the alloy-modified catalyst.

Oxygen vacancies function as crucial hubs in photocatalysis, promoting charge separation and activating reactant molecules [47]. To probe the mechanism of Cu-Bi alloys in CO_2 photoreduction, the concentration of oxygen vacancies was directly benchmarked among the catalysts by Electron Spin Resonance (ESR). As depicted in Figure 4d, the oxygen vacancy concentration in BT markedly exceeds that in pristine TiO_2. This enhancement stems from the mechanochemical reduction of TiO_2 by $NaBH_4$ during synthesis. Intensive grinding facilitates the cleavage of B-H bonds, releasing reactive hydrogen species (H•) or BH_4^- ions that directly reduce and extract lattice oxygen atoms from TiO_2, leading to the formation of oxygen vacancies [34]. The deposition of Cu or Bi SNCs significantly boosts the oxygen vacancy content of BT (Figure 4d). This enhancement originates from the strong metal-support interaction at the interface. The electronegativity mismatch between the metal atoms (Cu or Bi) and the TiO_2 support, coupled with the demand for interfacial bonding, induces additional local lattice distortion. To maintain charge balance and structural stability, this intense interfacial interaction drives the further reduction of the adjacent TiO_2 surface layer, thereby generating interfacial oxygen vacancies and resulting in an overall oxygen vacancy concentration higher than that of pristine BT. However, the oxygen vacancy concentration reaches its maximum upon loading Cu-Bi ASNCs. This phenomenon is due to the significant electronic interaction between the more electropositive (and oxophilic) Bi atoms and the Cu atoms within the alloy. This interaction induces a redistribution of electron density across the entire alloy cluster, which in turn intensifies the electron transfer at the interface with the BT support. To compensate for and stabilize this pronounced interfacial charge rearrangement, the BT surface spontaneously generates a greater number of oxygen vacancies, which serve as charge compensation centers[48]. Oxygen vacancies serve as highly efficient electron trapping centers that significantly suppress the recombination of photogenerated electron-hole pairs. In the Cu-Bi ASNCs, the oxophilicity of Bi combined with the electron-donating capability of Cu establishes an internal electronic coupling effect. This synergistic interaction drives the directional migration of photogenerated electrons from the TiO_2 bulk phase to the alloy active sites through oxygen vacancy-mediated pathways, thereby maximizing charge separation efficiency. Furthermore, oxygen vacancies

Just Accepted

function as preferential sites for CO_2 adsorption and activation. The localized electron enrichment at these vacancy sites effectively polarizes the C=O bonds, inducing a bent configuration transformation of the linear CO_2 molecule and significantly reducing the activation energy barrier. The high density of oxygen vacancies at the Cu-Bi alloy interface provides abundant active sites for the initial activation of CO_2. This integrated mechanism represents one of the primary reasons for the superior photocatalytic CO_2 reduction performance of the $Bi_{0.4}Cu_{0.6}$/BT catalyst.

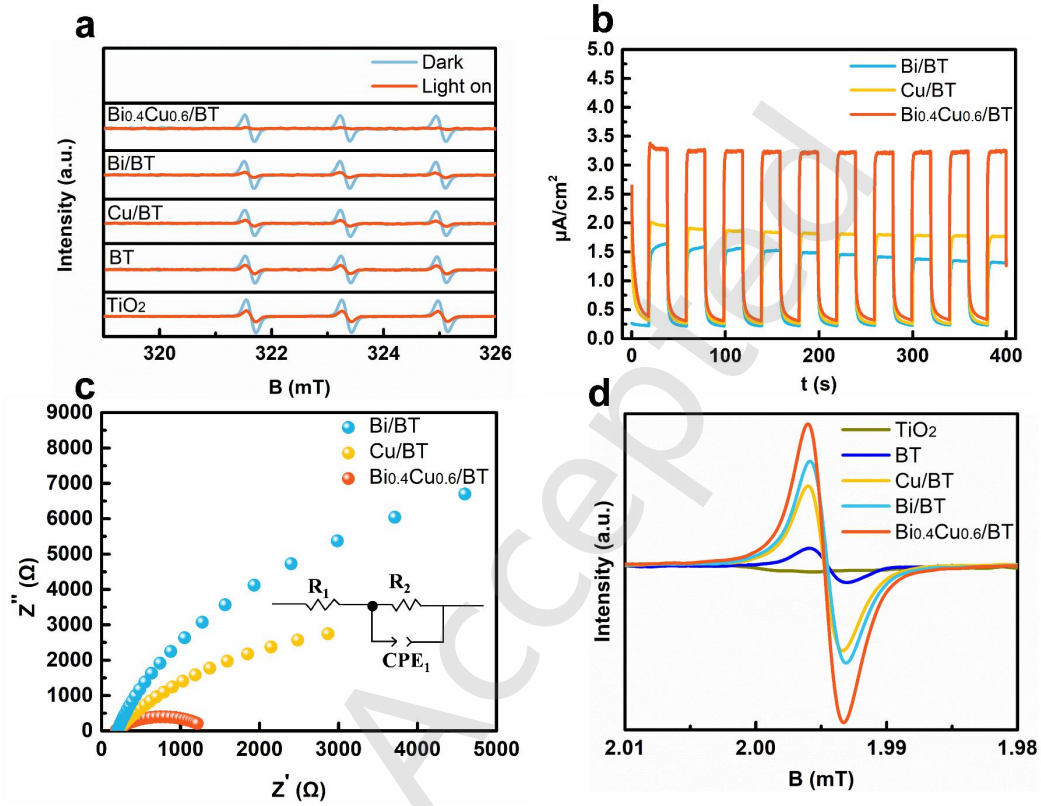


Figure 4. ESR spectra of photogenerated electrons recorded in the dark and under simulated solar irradiation for 10 minutes (a). Transient photocurrent densities under intermittent simulated solar irradiation (b). Nyquist plots of EIS spectra and the equivalent circuit (inset) (c). ESR spectra of oxygen vacancies in the dark (d).

3.4. Identification of the interface states

To elucidate the origin of the interfacial electronic structure, DFT calculations were performed to analyze the density of states for the Cu-Bi/BT system. As shown in Figure 5a, loading metal SNCs onto BT induces a positive shift in the total density of states (TDOS), signifying interfacial electron transfer and downward band bending. This effect raises the Fermi level and enhances the reducing capability of the composite [49, 50]. The projected density of states (PDOS) further resolves the orbital contributions to the interfacial states (IFS) within the BT bandgap. For Cu/BT (Figure 5b), the IFS arises from hybridization between Cu 3d electrons and adjacent O 2p/Ti 3d orbitals. Similarly, the Bi/BT system shows an IFS in the bandgap (Figure 5c), originating from charge donation by Bi 5d electrons to neighboring O 2p and Ti 3d orbitals. The projected density of states (PDOS) of Cu-Bi/BT initially reveals only the

Just Accepted

IFS generated by the interaction between Cu 3d and BT (Figure 5d), likely because the IFS intensity of Cu/BT is significantly stronger than that of Bi/BT, overshadowing the IFS signal from Bi. However, by amplifying the PDOS signals of Cu 4s, Cu 3p, and Cu 3d (Figure 5e), as well as Bi 6s, Bi 6p, and Bi 5d (Figure 5f), the IFS resulting from Bi-BT interaction becomes observable, confirming its presence in the Cu-Bi/BT. These results demonstrate that the Cu-Bi alloy establishes hybrid interfacial states with BT through concurrent Cu 3d and Bi 5d orbital interactions, thereby broadening the visible-light response beyond the intrinsic bandgap of the support.

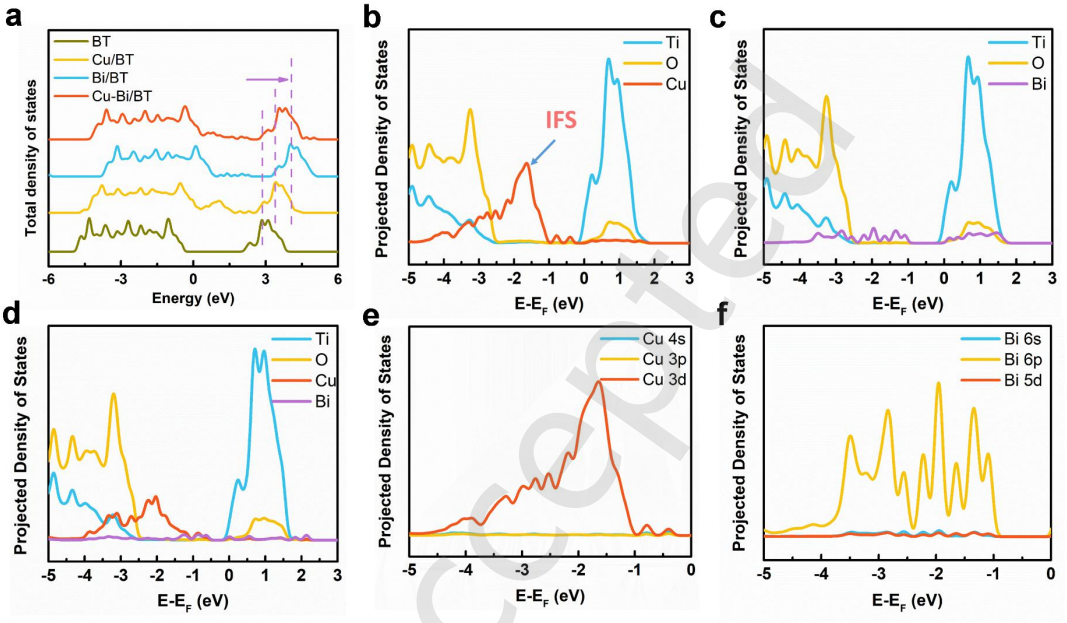


Figure 5. The total density of states (TDOS) for BT, Cu/BT, Bi/BT, and Cu-Bi/BT (a). The projected density of states (PDOS) for Cu/BT (b), Bi/BT (c) and Cu-Bi/BT (d). The PDOS for Cu 4s, Cu 3p and Cu 3d of Cu-Bi/BT (e). The PDOS for Bi 6s, Bi 6p and Bi 5d of Cu-Bi/BT (f).

3.5. Adsorption properties of the catalysts

The efficacy of photocatalytic CO_2 reduction is fundamentally governed by the catalyst's CO_2 adsorption properties. Effective adsorption initiates the process by concentrating reactant molecules at active sites. This is critical not only for enriching local CO_2 concentration but also for activating the molecules by weakening the C=O bonds, which reduces the activation energy for subsequent steps [51]. Moreover, strong adsorption is essential for enabling efficient charge transfer from the catalyst to the CO_2 molecules, a step that dictates the reaction pathway and final product distribution [52]. To elucidate these factors, the CO_2 adsorption characteristics of metal cocatalysts were systematically investigated using DFT calculations. As shown in Figure 6, for the Cu-Bi/BT catalyst, the adsorption energy of CO_2 on the Cu sites (-0.34 eV, Figure 6a) is significantly more negative than that on the Bi sites (-0.16 eV, Figure 6b), indicating stronger adsorption stability of CO_2 on the Cu sites within the Cu-Bi alloy. This is attributed to the higher d-band center and superior electron-donating capability of Cu compared to Bi, which enables more stable binding and effective activation of CO_2 molecules.

Just Accepted

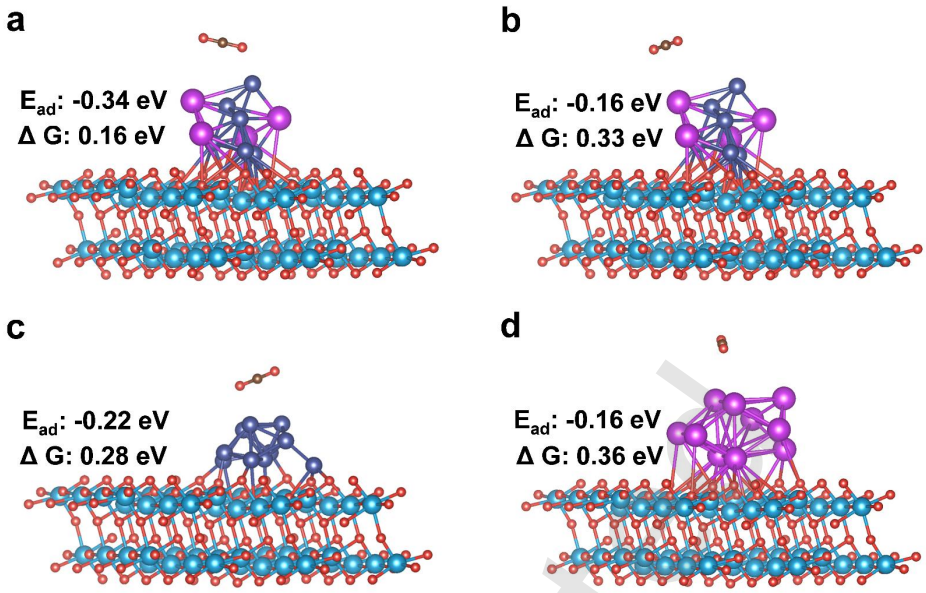


Figure 6. Optimized structures of CO_2 molecules absorbed on Cu in Cu-Bi alloy/BT (a), Bi in Cu-Bi alloy/BT (b), Cu in Cu/BT (c), Bi in Bi/BT (d), and their adsorption energies and Gibbs free energies. Ti, O, Cu, Bi, and C atoms are green, red, blue, pink, and brown spheres, respectively.

Notably, CO_2 adsorption on the Cu site of the Cu-Bi alloy/BT exhibits a Gibbs free energy change (ΔG) of 0.16 eV (Figure 6a), which is substantially lower than that on the Bi site (0.33 eV, Figure 6b). This energetic difference indicates that CO_2 adsorption on Cu sites is thermodynamically more favorable, requiring less energy input to proceed compared to adsorption on Bi sites. Adsorption on a Cu site in the pure Cu/BT catalyst (Figure 6c) yields an adsorption energy of -0.22 eV and a Gibbs free energy change of 0.28 eV. The notably enhanced adsorption energy and reduced Gibbs free energy barrier on the Cu site of the Cu-Bi alloy (-0.34 eV and 0.16 eV, respectively, in Figure 6a) underscore the synergistic effect of Cu and Bi within the alloy. The presence of Bi electronically modifies the Cu sites, making them thermodynamically more favorable for CO_2 adsorption than pure Cu. Meanwhile, CO_2 adsorption on a Bi site in the pure Bi/BT catalyst (Figure 6d) shows the least favorable thermodynamics (E_{ad} = -0.16 eV, ΔG = 0.36 eV), confirming that Bi in isolation is a poor adsorber of CO_2.

3.6. The reaction pathway of photocatalytic CO_2 reduction

To gain deeper insight into the reaction mechanism, *in situ* FT-IR spectroscopy was employed to track the evolution of intermediates during CO_2 reduction. Figure 7a demonstrates the formation of multiple adsorbed species on the $Bi_{0.4}Cu_{0.6}$/BT surface upon dark CO_2 and H_2O co-adsorption. Upon exposure of $Bi_{0.4}Cu_{0.6}$/BT to a mixture of CO_2 and H_2O in the absence of light, the catalyst surface became populated with various carbonaceous and hydrogenated species. These included monodentate carbonate (characterized by peak at 1284 cm^{-1}), bicarbonate (with features at 1427 cm^{-1}), as well as water molecules (showing a vibrational mode at 1639 cm^{-1}) [10, 14, 53-55]. Furthermore, under dark conditions, no distinct characteristic peaks

Just Accepted

corresponding to reaction intermediates were observed on the surfaces of the $Bi_{0.4}Cu_{0.6}$/BT (Figure 7a), Cu/BT (Figure 7b), and Bi/BT (Figure 7c) catalysts, suggesting that the reaction between $CO_2$and H_2O scarcely proceeds in the absence of light. Under simulated solar irradiation, several characteristic peaks corresponding to CO_2 reduction intermediates emerged on the surface of the $Bi_{0.4}Cu_{0.6}$/BT catalyst (Figure 7a), including those assignable to COOH* (1208 cm^{-1}), HCOOH* (1552 cm^{-1}), CH_2 * (1361 and 1478 cm^{-1}) and CH_3* (1380 cm^{-1}) [44, 56-62]. The variety and intensities of these intermediates fully encompass the stepwise hydrogenation pathway from CO_2 to CH_4, clearly delineating the evolution sequence of COOH* → HCOOH* → CH_2* → CH_3* → CH_4. These findings confirm that $Bi_{0.4}Cu_{0.6}$/BT possesses exceptional catalytic activity and selectivity for the reduction of CO_2 to CH_4. Upon illumination, key intermediate peaks corresponding to COOH* (1208 cm^{-1}), CH_2* (1355, 1478 cm^{-1}), and CH_3* (1382 cm^{-1}) were also detected on the Cu/BT catalyst (Figure 7b), with peak positions closely matching those of $Bi_{0.4}Cu_{0.6}$/BT, indicating that both follow the same CO_2 reduction pathway. However, compared with $Bi_{0.4}Cu_{0.6}$/BT, the overall intensities of the intermediate peaks on Cu/BT were significantly lower, while the CO_2^- peak at 1249 cm^{-1} was more pronounced, suggesting inferior efficiency in CO_2 activation and intermediate conversion. This result demonstrates that synergistic Bi doping effectively enhances the stabilization and enrichment of reaction intermediates at Cu sites, thereby promoting efficient CO_2-to-CH_4 conversion. For the Bi/BT catalyst (Figure 7c), only a few weak intermediate peaks were detected upon illumination, with intensities substantially lower than those of $Bi_{0.4}Cu_{0.6}$/BT and Cu/BT, indicating poor CO_2 reduction activity. This is likely due to insufficient CO_2 adsorption or a limited number of active sites on the Bi/BT surface, which hinders the effective generation and accumulation of intermediates, ultimately leading to inferior photocatalytic performance. Collectively, the *in situ* FT-IR results demonstrate that the synergistic Cu-Bi interaction in $Bi_{0.4}Cu_{0.6}$/BT underpins its exceptional CO_2 photoreduction performance by enabling full coverage of intermediates along the CO_2-to-CH_4 pathway, whereas Cu/BT suffers from compromised intermediate conversion in the absence of such synergy, and Bi/BT exhibits insufficient CO_2 activation owing to the lack of Cu-based active sites.

Just Accepted

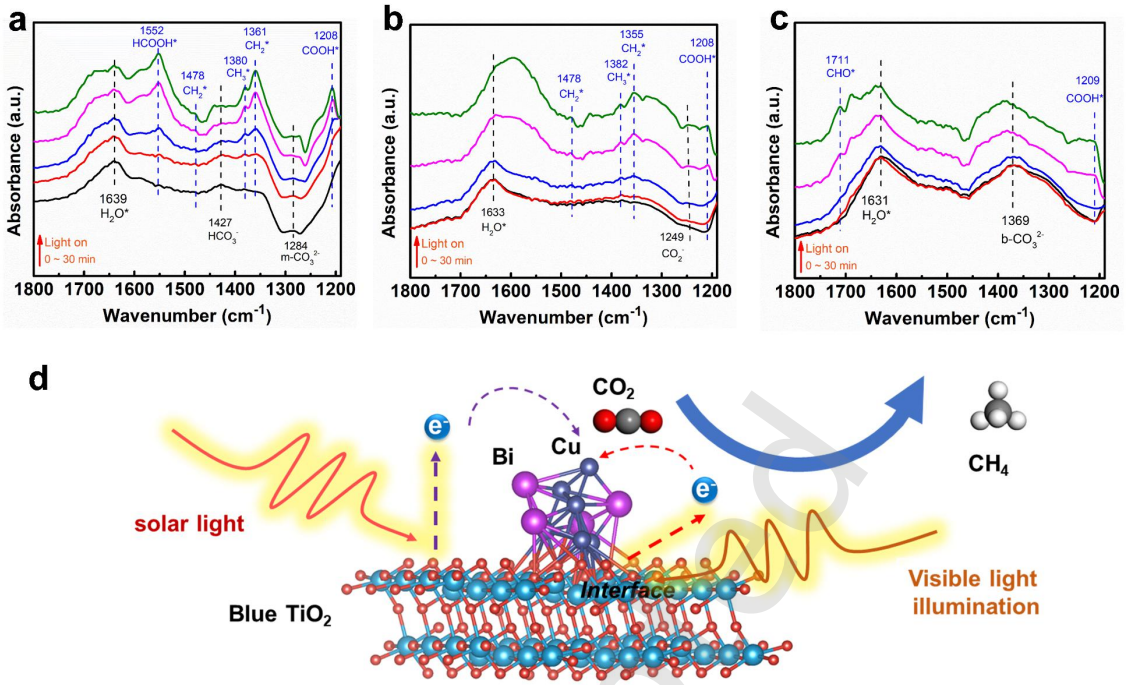


Figure 7. *In situ* FT-IR spectra of CO_2 and H_2O reaction on $Bi_{0.4}Cu_{0.6}$/BT (a), Cu/BT (b) and Bi/BT (c) under dark and light conditions. The curves from bottom to top represent adsorption for 30 minutes, and illumination for 2, 6, 16, and 30 minutes, respectively. Schematic illustration of CO_2 photoreduction process on Cu-Bi alloy/BT. Ti, O, Cu, Bi, and C atoms are green, red, blue, pink, and brown spheres, respectively.

Based on the above results, the CO_2 photoreduction mechanism of Cu-Bi ASNCs modified BT is proposed in Figure 7d. CO_2 molecules are preferentially adsorbed on the Cu active sites of Cu-Bi ASNCs, and the synergistic interaction between Cu and Bi can effectively improve the CO_2 adsorption and activation capability of the catalyst. The solar light excites the BT substrate to generate photogenerated electrons, while visible light induces the interface states at the interface between the BT support and Cu-Bi ASNCs to produce abundant hot electrons. Both photogenerated electrons and interfacial hot electrons rapidly migrate to the Cu-Bi active sites on the catalyst surface and provide sufficient electrons for CO_2 reduction. The Cu-Bi synergistic effect stabilizes the metallic active sites, accelerates the separation of photogenerated electron-hole pairs, promotes the generation and migration of interfacial hot electrons, and facilitates the adsorption and activation of CO_2, which accounts for the excellent photocatalytic performance of the catalyst.

4. Conclusions

In summary, we have successfully developed a facile stepwise photodeposition strategy for the controlled synthesis of Cu-Bi ASNCs with an average diameter of 0.84 ± 0.12 nm uniformly anchored on BT support, denoted as Bi_xCu_{1-x}/BT, for the photocatalytic reduction of CO_2 with H_2O. Under simulated solar irradiation, the optimally formulated $Bi_{0.4}Cu_{0.6}$/BT catalyst exhibits a CH_4 evolution rate of 94.4 μmol g^{-1} h^{-1} with a remarkable selectivity of 96.9%, substantially surpassing the photocatalytic performance of monometallic Cu/BT and Bi/BT counterparts. A combination of systematic experimental characterizations and density functional

Just Accepted

theory (DFT) calculations reveals that the synergistic interaction between Cu and Bi can inhibit the aerial oxidation of metallic Cu^0 and Bi^0, accelerate the separation of photogenerated electron-hole pairs, and facilitate the adsorption and activation of CO_2. Critically, the interfacial dielectric coupling between Cu-Bi ASNCs and BT induces IFS within the bandgap, which enables the direct generation of hot electrons upon visible-light excitation, thereby significantly enhancing the charge separation efficiency and overall photocatalytic activity. Moreover, the Cu-Bi alloy substantially lowers the Gibbs free energy barrier for CO_2 adsorption over Cu active sites and establishes a thermodynamically favorable pathway for stepwise hydrogenation of CO_2 toward CH_4. Collectively, this work demonstrates a non-noble-metal alloy sub-nanocluster strategy for efficient and selective photocatalytic CO_2-to-CH_4 conversion. The mechanistic insights into interfacial charge dynamics, oxygen vacancy engineering, and the synergistic effects within alloy-decorated defective semiconductor systems may inform the design of related photocatalyst systems.

Electronic Supplementary Material

Supplementary material including detailed DFT calculation parameters, HAADF and HAADF-STEM images, XRD patterns, UV-vis DRS spectra, photocatalytic activity data, cycling stability tests, and ESR characterizations (Figures S1-S8) is available online at https://doi.org/10.26599/NR.2026.94909225.

Data availability

All data needed to support the conclusions in the paper are presented in the manuscript and the Electronic Supplementary Material. Additional data related to this paper may be requested from the corresponding author upon request.

Acknowledgments

This work was supported by the National Natural Science Foundation of China (22308191, 22361142703, 52570120).

Declaration of competing interest

The authors declare no competing financial interests.

Author contribution statement

Y. Y. Yu.: Conceptualization, funding acquisition, methodology, investigation, data curation, validation, visualization, writing manuscript. Y. J. Sun.: Conceptualization, resources, funding acquisition, project administration, supervision, formal analysis, writing-review & editing. F. Dong.: Resources, funding acquisition, project administration, supervision, writing-review & editing. All the authors have approved the final manuscript.

Informed consent

Not applicable

Ethics statement

Not applicable

Use of AI statement

None.

References

[1] Rao, H.; Chmidt, L. C. S.; Bonin, J.; Robert, M.

Just Accepted

Visible-light-driven methane formation from CO_2 with a molecular iron catalyst. *Nature.* **2017**, *548*, 74-77.

[2] Hepburn, C.; Adlen, E.; Beddington, J.; Carter, E. A.; Fuss, S.; Mac Dowell, N.; Minx, J. C.; Smith, P.; Williams, C. K. The technological and economic prospects for CO_2 utilization and removal. *Nature.* **2019**, *575*, 87-97.

[3] Guo, Z.; Chen, G.; Cometto, C.; Ma, B.; Zhao, H.; Groizard, T.; Chen, L.; Fan, H.; Man, W. L.; Yiu, S. M. Selectivity control of CO versus $HCOO^-$ production in the visible-light-driven catalytic reduction of CO_2 with two cooperative metal sites. *Nat. Catal.* **2019**, *2*, 801-808.

[4] Zhang, T.; Han, X.; Nguyen, N.T.; Yang, L.; Zhou, X. TiO_2-based photocatalysts for CO_2 reduction and solar fuel generation, Chin. J. Catal. **2022,** *43*, 2500-2529.

[5] Ran, J.; Jaroniec, M.; Qiao, S. Z. Cocatalysts in semiconductor‐based photocatalytic CO_2 reduction: achievements, challenges, and opportunities. *Adv. Mater.* **2018**, *30*, 1704649.

[6] Gao, G.; Jiao, Y.; Waclawik, E. R.; Du, A. Single atom (Pd/Pt) supported on graphitic carbon nitride as an efficient photocatalyst for visible-light reduction of carbon dioxide. *J. Am. Chem. Soc.* **2016**, *138*, 6292-6297.

[7] Cao, L.; Sahu, S.; Anilkumar, P.; Bunker, C. E.; Xu, J.; Fernando, K. S.; Wang, P.; Guliants, E. A.; Tackett, K. N.; Sun, Y.-P. Carbon nanoparticles as visible-light photocatalysts for efficient CO_2 conversion and beyond. *J. Am. Chem. Soc.* **2011**, *133*, 4754-4757.

[8] Ross, M. B.; De Luna, P.; Li, Y.; Dinh, C. T.; Kim, D.; Yang, P.; Sargent, E. H. Designing materials for electrochemical carbon dioxide recycling. *Nat. Catal.* **2019**, *2*, 648-658.

[9] Wang, M.; Shen, M.; Jin, X.; Tian, J.; Li, M.; Zhou, Y.; Zhang, L.; Li, Y.; Shi, J. Oxygen vacancy generation and stabilization in CeO_{2-x} by Cu introduction with improved CO_2 photocatalytic reduction activity. *ACS Catal.* **2019**, *9*, 4573-4581.

[10] Li, Y.; Li, B.; Zhang, D.; Cheng, L.; Xiang, Q. Crystalline carbon nitride supported copper single atoms for photocatalytic CO_2 reduction with nearly 100% CO Selectivity. *ACS Nano.* **2020**. *14*, 10552-10561.

[11] Jiang, Z.; Sun, W.; Miao, W.; Yuan, Z.; Yang, G.; Kong, F.; Yan, T.; Chen, J.; Huang, B.; An, C.; et al. Living atomically dispersed Cu ultrathin TiO_2 nanosheet CO_2 reduction photocatalyst. *Adv. Sci.* **2019**, *6*, 1900289.

[12] Zhang, X.; Han, F.; Shi, B.; Farsinezhad, S.; Dechaine, G. P.; Shankar, K. Photocatalytic conversion of diluted CO_2 into light hydrocarbons using periodically modulated multiwalled nanotube arrays. *Angew. Chem. Int. Ed.* **2012**, *51*, 12732-12735.

[13] Long, R.; Li, Y.; Liu, Y.; Chen, S.; Zheng, X.; Gao, C.; He, C.; Chen, N.; Qi, Z.; Song, L. Isolation of Cu atoms in Pd lattice: forming highly selective sites for photocatalytic conversion of CO_2 to CH_4. *J. Am. Chem. Soc.* **2017**, *139*, 4486-4492.

[14] Neaţu, S. t.; Maciá-Agulló, J. A.; Concepción, P.; Garcia, H. Gold-copper nanoalloys supported on TiO_2 as photocatalysts for CO_2 reduction by water, *J. Am. Chem. Soc.* **2014,** *136*, 15969-15976.

[15] Lee, S.; Jeong, S.; Kim, W. D.; Lee, S.; Lee, K.; Bae, W. K.; Moon, J. H.; Lee, S.; Lee, D. C. Low-coordinated surface atoms of CuPt alloy cocatalysts on TiO_2 for enhanced photocatalytic conversion of CO_2. *Nanoscale.* **2016**, *8*, 10043-10048.

[16] Yu, Y.; Dong, X. a.; Chen, P.; Geng, Q.; Wang, H.; Li, J.; Zhou, Y.; Dong, F. Synergistic effect of Cu single atoms and Au–Cu alloy nanoparticles on TiO_2 for efficient CO_2 photoreduction. *ACS Nano.* **2021**, *15*, 14453-14464.

[17] Yang, G.; Miao, W.; Yuan, Z.; Jiang, Z.; Huang, B.; Wang, P.; Chen, J. Bi quantum dots obtained via in situ photodeposition method as a new photocatalytic CO_2 reduction cocatalyst instead of noble metals: Borrowing redox conversion between Bi_2O_3 and Bi. *Appl. Catal. B Environ.* **2018**, *237*, 302-308.

[18] Gu, J.; Guo, R.; Miao, Y.; Liu, Y.; Wu, G.; Duan, C.; Pan, W. Noble-metal-free Bi/g-C_3N_4 nanohybrids for efficient photocatalytic CO_2 reduction under simulated irradiation. *Energ Fuel.* **2021**, *35*, 10102-10112.

[19] Zhu, J.; Li, Y.; Wang, X.; Zhao, J.; Wu, Y.; Li, F. Simultaneous phosphorylation and Bi modification of BiOBr for promoting photocatalytic CO_2 reduction. *ACS Sustainable Chem. Eng.* **2019**, *7*, 14953-14961.

[20] Huang, L.; Duan, Z.; Song, Y.; Li, Q.; Chen, L. $BiVO_4$ Microplates with oxygen vacancies decorated with metallic Cu and Bi nanoparticles for CO_2 photoreduction. *ACS Appl. Nano Mater.* **2021**, *4*, 3576-3585.

[21] Kang, X.; Li, Y.; Zhu, M.; Jin, R. Atomically precise alloy nanoclusters: syntheses, structures, and properties. *Chem. Soc. Rev.* **2020**, *49*, 6443-6514.

[22] Campbell, C. T.; Parker, S. C.; Starr, D. E. The effect of size-dependent nanoparticle energetics on

Just Accepted

catalyst sintering. *Science.* **2002**, *298*, 811-814.

[23] Hu, Q.; Han, Z.; Wang, X.; Li, G.; Wang, Z.; Huang, X.; Yang, H.; Ren, X.; Zhang, Q.; Liu, J. Facile synthesis of sub‐nanometric copper clusters by double confinement enables selective reduction of carbon dioxide to methane. *Angew. Chem. Int. Ed.* **2020**, *59*, 19054-19059.

[24] Zhang, X.; Liu, J. X.; Zijlstra, B.; Filot, I. A.; Zhou, Z.; Sun, S.; Hensen, E. J. Optimum Cu nanoparticle catalysts for CO_2 hydrogenation towards methanol. *Nano Energy.* **2018**, *43*, 200-209.

[25] Liu, L.; Corma, A. Metal catalysts for heterogeneous catalysis: from single atoms to nanoclusters and nanoparticles. *Chem. Rev.* **2018**, *118*, 4981-5079.

[26] Zou, S.; Lou, B.; Yang, K.; Yuan, W.; Zhu, C.; Zhu, Y.; Du, Y.; Lu, L.; Liu, J.; Huang, W. Grafting nanometer metal/oxide interface towards enhanced low-temperature acetylene semi-hydrogenation. *Nat. Commun.* **2021**, *12*, 1-11.

[27] Tan, S.; Argondizzo, A.; Ren, J.; Liu, L.; Zhao, J.; Petek, H. Plasmonic coupling at a metal/semiconductor interface. *Nat. Photonics.* **2017**, *11*, 806-812.

[28] Collado, L.; Reynal, A.; Fresno, F.; Barawi, M.; Escudero, C.; Perez-Dieste, V.; Coronado, J. M.; Serrano, D. P.; Durrant, J. R.; de la Peña O'Shea, V. A. Unravelling the effect of charge dynamics at the plasmonic metal/semiconductor interface for CO_2 photoreduction. *Nat. Commun.* **2018**, *9*, 1-10.

[29] Yu, Y.; He, Y.; Yan, P.; Wang, S.; Dong, F. Boosted C-C coupling with Cu-Ag alloy sub-nanoclusters for CO_2-to-C_2H_4 photosynthesis. *Proc. Natl. Acad. Sci. U.S.A.* **2023**, *120*, e2307320120.

[30] Chen, J.; Shuai, J.; Chen, X.; Du, J.; Zhao, B.; Yu, X.; Feng, W.; Zheng, G.; Wu, X.; Zhou, X. Chiral plasmonic nanocatalysts for enhanced CO_2 methanation activity and selectivity via polarized photogenerated hot carriers. *Nano Research.* **2025**, *18*, 94907940.

[31] Boucher, M. B.; Zugic, B.; Cladaras, G.; Kammert, J.; Marcinkowski, M. D.; Lawton, T. J.; Sykes, E. C. H.; Flytzani-Stephanopoulos, M. Single atom alloy surface analogs in $Pd_{0.18}Cu_{15}$ nanoparticles for selective hydrogenation reactions. *Phys. Chem. Chem. Phys.* **2013**, *15*, 12187-12196.

[32] Ge, M.; Huang, J.; Tian, Y.; Zhou, L.; Li, H.; Zhang, A.; Zhu, S.; Zhu, X.; Li, Q.; Min, Y. Electrodeposition-Assisted Crystal Growth Regulation of PdBi Clusters on Carbon Cloths for Ethanol Oxidation. *Inorg. Chem.* **2023**, *62*, 15138-15147.

[33] Pennycook, S. J.; Jesson, D. E. High-resolution Z-contrast imaging of crystals. *Ultramicroscopy.* **1991**, *37*, 14-38.

[34] Sorcar, S.; Hwang, Y.; Grimes, C. A.; In, S. I. Highly enhanced and stable activity of defect-induced titania nanoparticles for solar light-driven CO_2 reduction into CH_4. *Mater. Today.* **2017**, *20*, 507-515.

[35] Desario, P. A.; Pietron, J. J.; Brintlinger, T. H.; Mcentee, M.; Parker, J. F.; Baturina, O.; Stroud, R. M.; Rolison, D. R. Oxidation-stable plasmonic copper nanoparticles in photocatalytic TiO_2 nanoarchitectures. *Nanoscale.* **2017**, *9*, 11720-11729.

[36] Jing, Q.; Feng, X.; Pan, J.; Chen, L.; Liu, Y. Facile synthesis of $Bi/BiVO_4$ composite ellipsoids with high photocatalytic activity. *Dalton T.* **2018**, *47*, 2602-2609.

[37] Xu, H.; Zhang, K.; Yan, B.; Wang, J.; Wang, C.; Li, S.; Gu, Z.; Du, Y.; Yang, P. Ultra-uniform PdBi nanodots with high activity towards formic acid oxidation. *J. Power Sources.* **2017**, *356*, 27-35.

[38] Huang, J.; Ding, T.; Ma, K.; Cai, J.; Sun, Z.; Tian, Y.; Jiang, Z.; Zhang, J.; Zheng, L.; Li, X. Modification of Cu/SiO_2 Catalysts by La_2O_3 to quantitatively tune Cu^+-Cu^0 dual sites with improved catalytic activities and stabilities for dimethyl ether steam reforming. *ChemCatChem.* **2018**, *10*, 3862-3871.

[39] Chen, Y.; Agrelo‐Lestón, A.; Burgués‐Ceballos, I.; Llorca, J.; Soler, L. Bimetallic Nanoparticles as Cocatalysts for Photocatalytic Hydrogen Production. *Adv. Funct. Mater.* **2026**, *36*, e06279.

[40] Gebre, S. H.; Sendeku, M. G. Trimetallic nanostructures and their applications in electrocatalytic energy conversions. *J. Energy Chem.* **2022**, *65*, 329-351.

[41] Wu, Z. P.; Shan, S.; Xie, Z.; Kang, N.; Park, K.; Hopkins, E.; Yan, S.; Sharma, A.; Luo, J.; Wang, J. Revealing the role of phase structures of bimetallic nanocatalysts in the oxygen reduction reaction. *ACS Catal.* **2018**, *8*, 11302-11313.

[42] Deng, F.; Li, N.; Tang, S.; Liu, C.; Yue, H.; Liang, B. Evolution of active sites and catalytic consequences of mesoporous MCM-41 supported copper catalysts for the hydrogenation of ethylene carbonate. *Chem. Eng. J.* **2018**, *334*, 1943-1953.

[43] Zhang, R.; Wang, H.; Tang, S.; Liu, C.; Dong, F.; Yue, H.; Liang, B. Photocatalytic oxidative dehydrogenation of ethane using CO_2 as a soft oxidant

Just Accepted

over Pd/TiO_2 catalysts to C_2H_4 and syngas. *ACS Catal.* **2018**, *8*, 9280-9286.

[44] Sangpour, P.; Hashemi, F.; Moshfegh, A. Z. Photoenhanced degradation of methylene blue on cosputtered M: TiO_2 (M= Au, Ag, Cu) nanocomposite systems: a comparative study. *J. Phys. Chem. C.* **2010**, *114*, 13955-13961.

[45] Xiang, P.; Wang, L.; Geng, Q.; Guo, C.; Xie, H.; Li, Y.; Yu, Y.; Wang, J. Improvement of efficiency and selectivity of CO_2 photoreduction over $Bi_2O_2SO_4$ catalysts with Cu-Bi alloys. *Surf. Interfaces.* **2025**, *62*, 106192.

[46] Yu, Y.; Zhu, Y.; Guo, J.; Yue, H.; Zhang, H.; Liang, B. Suppression of TiO_2 photocatalytic activity by low-temperature pulsed CVD-grown SnO_2 protective layer. *Ind. Eng. Chem.Res.* **2018**, *57,* 8679-8688.

[47] Liu, G.; Wang, X.; Chen, Z.; Cheng, H. M.; Lu, G. Q. M. The role of crystal phase in determining photocatalytic activity of nitrogen doped TiO_2. *J. Colloid Interf. Sci.* **2009**, *329*, 331-338.

[48] Yang, L.; Du, J.; Deng, J.; Sulaiman, N. H. M.; Feng, X.; Liu, C.; Zhou, X. Defective Nb_2C MXene cocatalyst on TiO_2 microsphere for enhanced photocatalytic CO_2 conversion to methane. *Small.* **2024**, *20*, 2307007.

[49] Leybo, D.; Etim, U. J.; Monai, M.; Bare, S. R.; Zhong, Z.; Vogt, C. Metal-support interactions in metal oxide-supported atomic, cluster, and nanoparticle catalysis. *Chem. Soc. Rev.* **2024**. *53*, 10450 -10490.

[50] Ullah, F.; Mohamed, N.; Ghani, U.; Saheed, M. First principle DFT+ U calculations for the optoelectronic properties of Cu and C-Cu co-doped TiO_2 anatase model. *Asian J. Chem.* **2022**, *34*, 1863-1868.

[51] Bo, Y.; Gao, C.; Xiong, Y. Recent advances in engineering active sites for photocatalytic CO_2 reduction. *Nanoscale.* **2020**, *12*, 12196-12209.

[52] Aslam, M. K.; Hussain, I.; Al-Marzouqi, A. H.; Xu, M. Advances in covalent organic frameworks for photocatalytic CO_2 reduction: Strategies and future perspectives. *Nano Res. Energy.* **2025**, *4*, e9120149.

[53] Yang, X.; Wang, S.; Yang, N.; Zhou, W.; Wang, P.; Jiang, K.; Li, S.; Song, H.; Ding, X.; Chen, H.; et al. Oxygen vacancies induced special CO_2 adsorption modes on Bi_2MoO_6 for highly selective conversion to CH_4. *Appl. Catal. B Environ.* **2019**, *259*, 118088.

[54] Liu, L.; Zhao, C.; Miller, J. T.; Li, Y. Mechanistic study of CO_2 photoreduction with H_2O on Cu/TiO_2 nanocomposites by *in situ* X-ray absorption and infrared spectroscopies. *J. Phys. Chem. C.* **2016**, *121*, 490-499.

[55] Di, T.; Zhu, B.; Cheng, B.; Yu, J.; Xu, J. A direct Z-scheme g-C_3N_4/SnS_2 photocatalyst with superior visible-light CO_2 reduction performance. *J. Catal.* **2017**, *352*, 532-541.

[56] Tang, J.; Guo, R.; Pan, W.; Zhou, W.; Huang, C. Visible light activated photocatalytic behaviour of Eu (III) modified g-C_3N_4 for CO_2 reduction and H_2 evolution. *Appl. Surf. Sci.* **2019**, *467*, 206-212.

[57] Wu, J.; Li, X.; Shi, W.; Ling, P.; Sun, Y.; Jiao, X.; Gao, S.; Liang, L.; Xu, J.; Yan, W.; et al. Efficient visible-light-driven CO_2 reduction mediated by defect-engineered BiOBr atomic layers. *Angew. Chem. Int. Ed.* **2018**, *57*, 8719-8723.

[58] Luan, Z.; Fournier, J. A. *In situ* FTIR spectroscopic investigation of active sites and adsorbate interactions in mesoporous aluminosilicate SBA-15 molecular sieves. *Micropor. Mesopor. Mat.* **2005**, *79*, 235-240.

[59] Wang, J.; Li, G.; Li, Z.; Tang, C.; Feng, Z.; An, H.; Liu, H.; Liu, T.; Li, C. A highly selective and stable ZnO-ZrO_2 solid solution catalyst for CO_2 hydrogenation to methanol. *Sci. Adv.* **2017**, *3*, e1701290.

[60] Li, N.; Jiang, R.; Li, Y.; Zhou, J.; Ma, Q.; Shen, S.; Liu, M. Plasma-assisted Photocatalysis of CH_4 and CO_2 into Ethylene. *ACS Sustain. Chem. Eng.* **2019**, *7*, 11455-11463.

[61] Cho, L.; Huang, K. Identification of condom lubricants by FT-IR Spectroscopy. *Forensic Sci. J.* **2012**, *11*, 33-40.

[62] Murcia, J.; Hidalgo, M. C.; Navío, J. A.; Araña, J.; Doña-Rodríguez, J. *In situ* FT-IR study of the adsorption and photocatalytic oxidation of ethanol over sulfated and metallized TiO_2. *Appl. Catal. B Environ.* **2013**, *142*, 205-213.

Just Accepted

Electronic Supplementary Material

Synergistic Cu-Bi alloy sub-nanoclusters anchored on blue TiO_2 for selective CO_2 photoreduction to CH_4

Yangyang Yu [1], Yanjuan Sun [2] ✉, Fan Dong [2]

[1] *Research Institute for Carbon Dioxide Resource Utilization, Tianfu Yongxing Laboratory, Chengdu 610213, China*

[2] *School of Resources and Environment, Institute of Fundamental and Frontier Sciences, University of Electronic Science and Technology of China, Chengdu 611731, China*

✉ Address correspondence to sunyj@uestc.edu.cn

Supporting information to https://doi.org/10.26599/NR.2026.94909225

Just Accepted

DFT calculation details

The spin-polarized density functional theory (DFT) calculations were performed using the Vienna Ab initio Simulation Package (VASP 5.4.1) with the generalized gradient approximation (GGA) in the Perdew-Burke-Ernzerhof (PBE) exchange-correlation functional. Model construction: A 4 × 4 anatase TiO_2 (101) supercell (3 atomic layers, bottom layer fixed) with a 15 Å vacuum slab was constructed. Monometallic Cu_{10} and Bi_{10} clusters, as well as Cu_6Bi_4 alloy clusters (as depicted in Figure 6), were anchored on the oxygen-vacancy site of BT. A 3×3×1 k-point mesh was employed for sampling the Brillouin zone. Structural relaxation was considered converged when the forces on all ions were below 0.03 eV/Å, and the energy convergence criterion was set to 10^{-4} eV. The Bader method was used to calculate the electron transfer quantity (Δq). The Gibbs free energy for CO_2 photoreduction was computed at 298.15 K, according to the equation $G = E_{DFT} + E_{ZPE} - TS$, where E_{DFT}, E_{ZPE}, and TS are the electronic energy, zero-point energy, and entropy contribution, respectively. Solvent and atmosphere approximation: The CO_2 adsorption calculations were performed in the gas phase without explicit H_2O vapor, as the primary objective was to evaluate the intrinsic adsorption energy on metal active sites. The effect of H_2O was implicitly considered via the Gibbs free energy correction at 298.15 K and 90 kPa.

Just Accepted

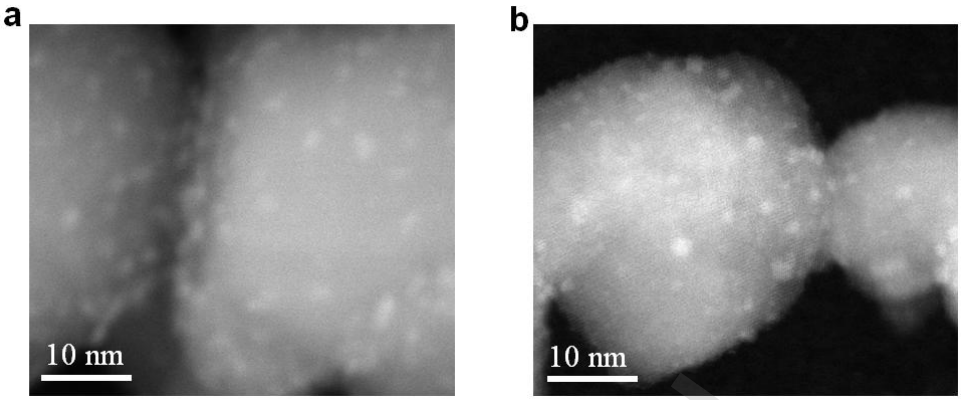


Figure S1. HAADF images of Bi/BT (a) and Cu/BT (b).

Just Accepted

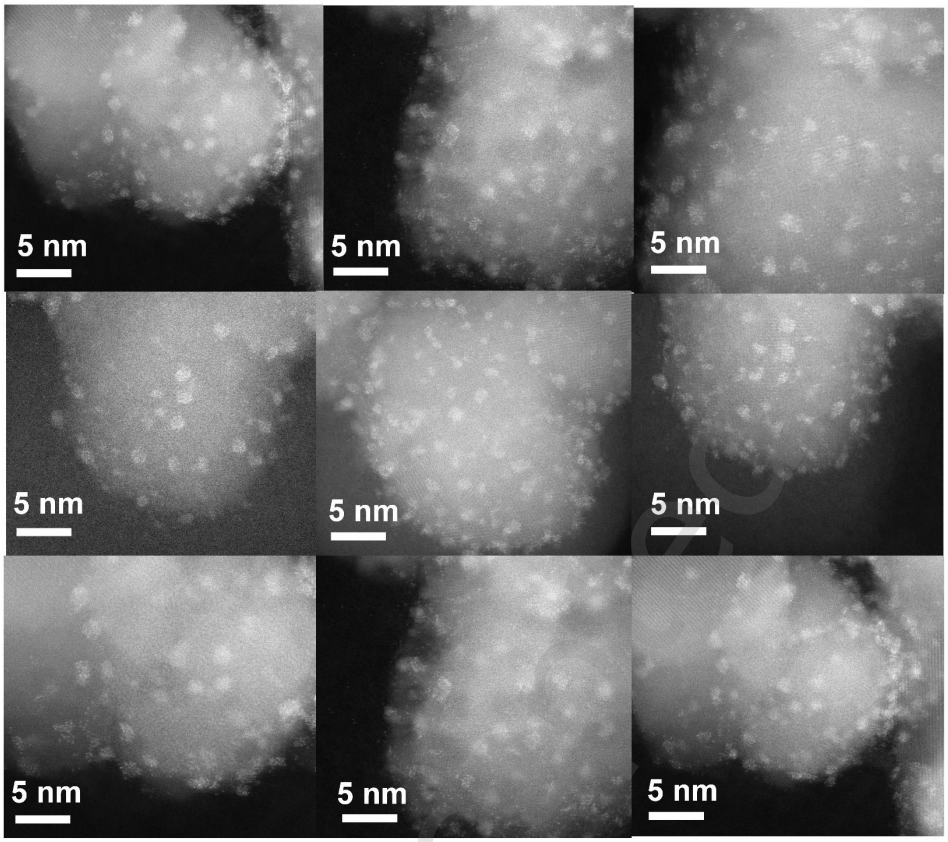


Figure S2. HAADF-STEM images of $Bi_{0.4}Cu_{0.6}$/BT.

Just Accepted

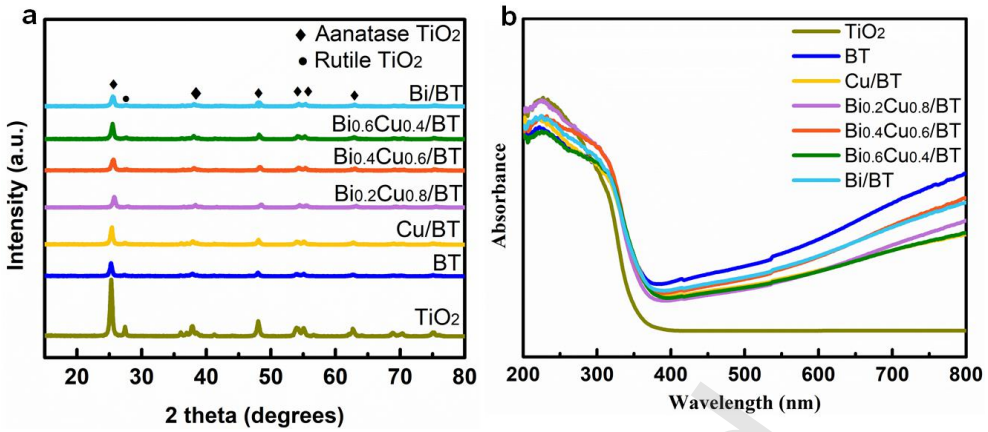


Figure S3. XRD pattern (a) and UV-vis DRS spectra (b) of the catalysts.

Just Accepted

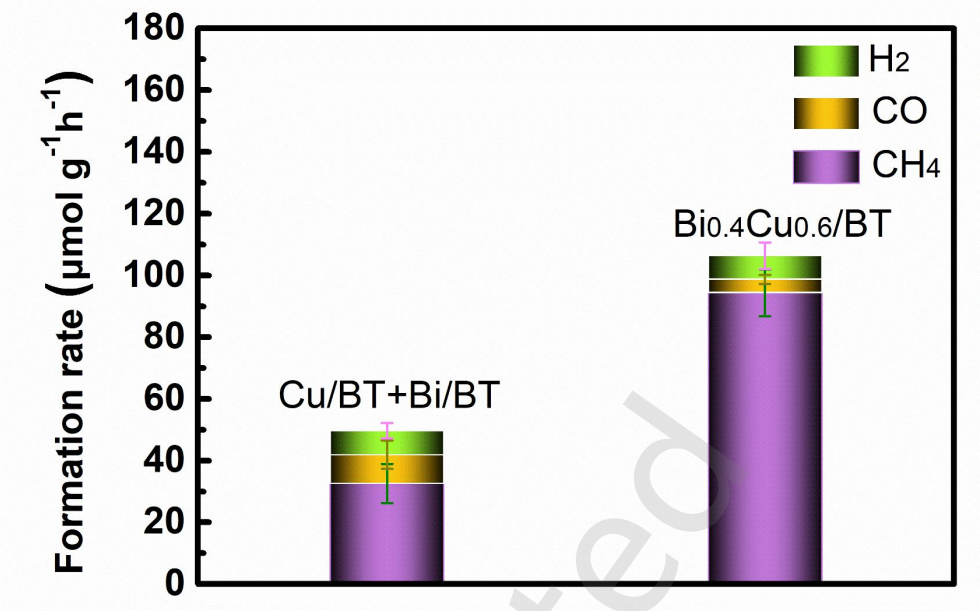


Figure S4. CH_4, H_2 and CO formation rates over Cu/BT + Bi/BT and $Bi_{0.4}Cu_{0.6}$/BT under 5 h simulated solar (AM 1.5G) irradiation. Data are presented as the average of three independent measurements, and the error bars represent the standard deviation.

Just Accepted

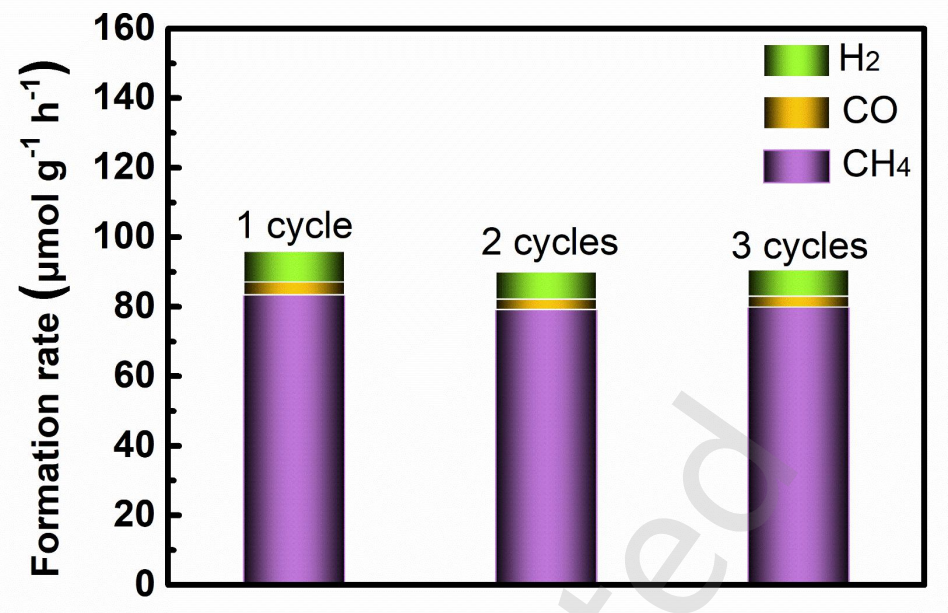


Figure S5. Three-cycle test of the photocatalytic CO_2 reduction activity of $Bi_{0.4}Cu_{0.6}$/BT in the presence of simulated solar (AM 1.5G) irradiation. Each cycle was tested for 10 h.

Just Accepted

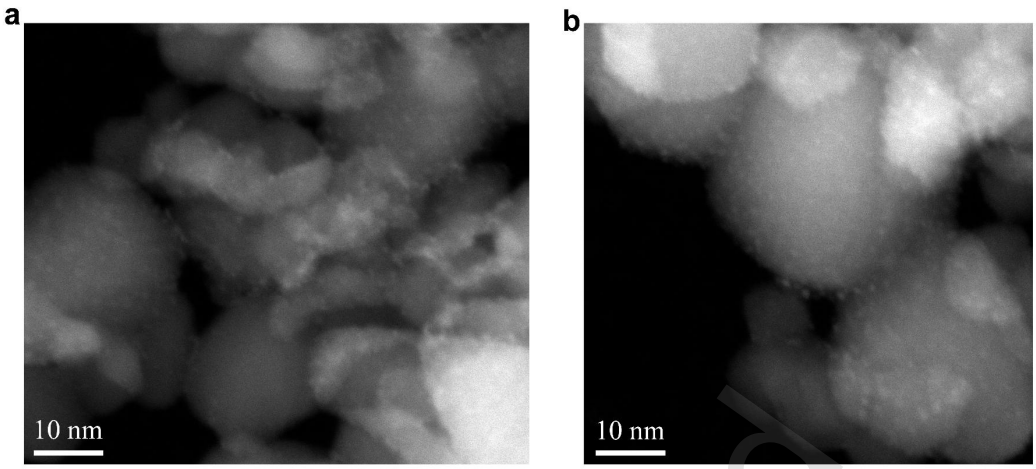


Figure S6. HAADF images of fresh $Bi_{0.4}Cu_{0.6}$/BT (a) and post-reaction $Bi_{0.4}Cu_{0.6}$/BT (b) recovered after three consecutive 10 h photocatalytic CO_2 reduction cycles under simulated solar irradiation.

Just Accepted

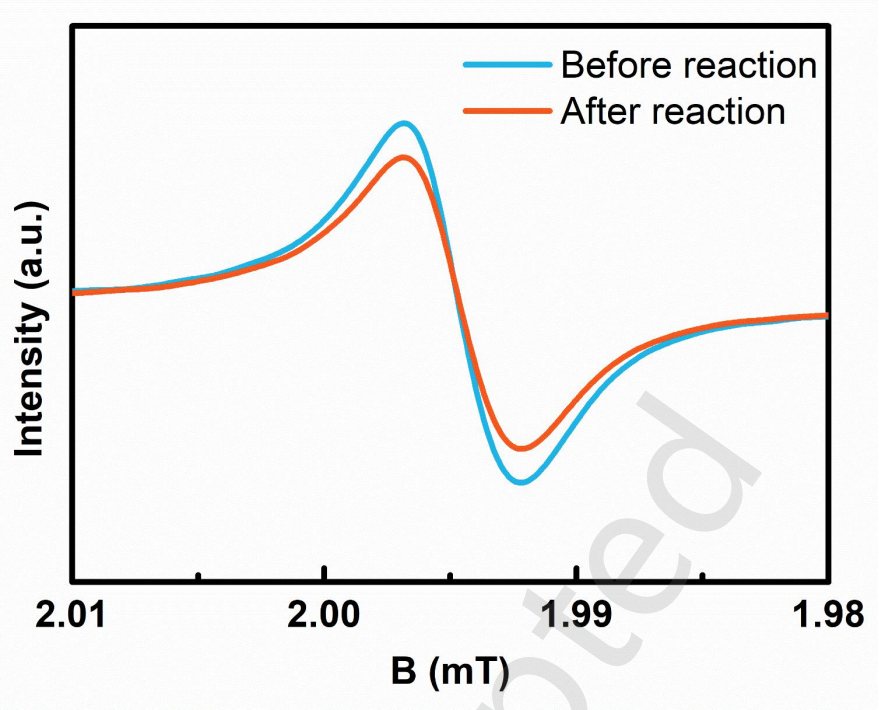


Figure S7. ESR spectra of oxygen vacancies in fresh and post-reaction $Bi_{0.4}Cu_{0.6}$/BT (recovered after three consecutive 10 h cycles).

Just Accepted

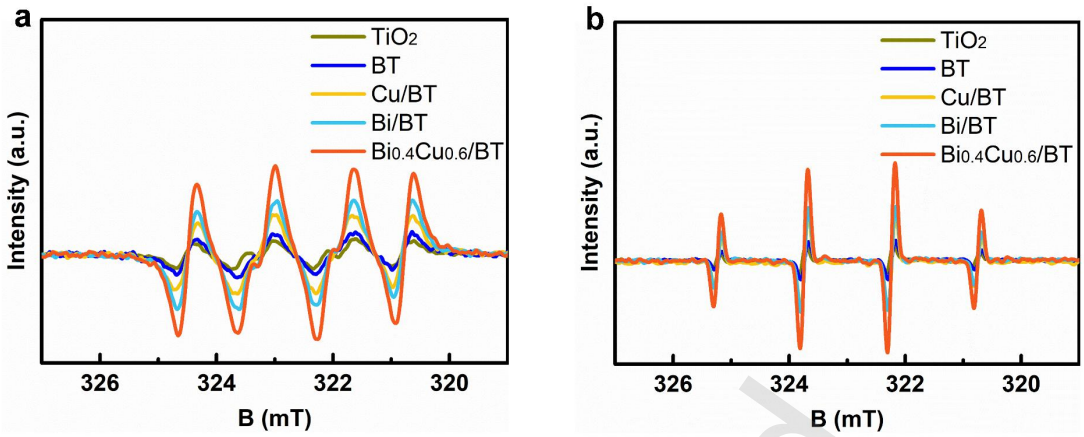


Figure S8. DMPO ESR spectra in the dark and under simulated sunlight for 10 min for $\bullet O^{2-}$ (a) and •OH (b).

Just Accepted